



Available online at www.sciencedirect.com

ScienceDirect

Proceedings
of the
Combustion
Institute

Proceedings of the Combustion Institute 38 (2021) 2517–2524

www.elsevier.com/locate/proci

Spatially resolved measurements of soot and gaseous precursors in ethylene counterflow diffusion flames up to 32 atm

Kevin Gleason ^a, Francesco Carbone ^{a,b}, Alessandro Gomez ^{a,*}

^a Yale Center for Combustion Studies, Department of Mechanical Engineering and Materials Science, Yale University, 9 Hillhouse Avenue, New Haven, CT 06520-8286, USA

Received 6 November 2019; accepted 20 June 2020 Available online 2 September 2020

Abstract

We investigate the effect of pressure on both flame structure and soot formation in nitrogen diluted counterflow diffusion flames of ethylene in the 8-32atm pressure range. Capillary-probe gas sampling is performed to resolve spatially the profiles of gaseous species up to three-ring aromatics by GC/MS analysis and multicolor pyrometry is used to quantify the soot volume fraction and dispersion exponent. Self-similarity of flames is preserved by keeping constant mixture fraction and strain rate, so that profiles of concentrations and temperature, normalized with respect to their peak values, are unaffected by changes in pressure, once the axial coordinate is nondimensionalized with respect to the pressure-dependent diffusion length scale. When conditions are chosen so that the overall soot loading is approximately constant and compatible with the diagnostics, it is found that both the soot volume fraction and the profiles of key aromatics in the hightemperature nucleation region are virtually invariant. For it to happen, a twofold increase in pressure must be compensated by a ~100 K decrease in peak flame temperature and, therefore, in the temperature across the soot forming region. The implication is that from the perspective of the chemical kinetics of soot formation these two actions counterbalance each other. As pressure increases (and temperature decreases) the peak production rate of the high-temperature soot mechanism decreases and, further downstream, towards the particle stagnation plane, a low-temperature soot mechanism sets in, yielding an increase in soot H/C content. This mechanism is enhanced as the pressure is raised, causing a higher overall soot volume production rate in the 16atm flame and, especially, in the 32atm one. The role of C4/C2 species in the formation of C_6H_6 increases with increasing pressure and dominates over the recombination of propargyl radical at sufficiently high pressures. A comprehensive database is established for soot models at high pressures of relevance to applications.

© 2020 Published by Elsevier Inc. on behalf of The Combustion Institute.

Keywords: Soot formation; High pressure; Diffusion flames; Counterflow

E-mail address: alessandro.gomez@yale.edu (A. Gomez).

^b Department of Mechanical Engineering, University of Connecticut, 191 Auditorium Road, Unit 3139, Storrs, CT 06269-3139, USA

^{*} Corresponding author.

1. Introduction

The study of soot formation has been the focus of research for decades, as reviewed in [1–4]. Despite its long history, one aspect, the gas-toparticle transition, remains poorly understood. The difficulty lies in the need for complementary diagnostics to quantify both gas phase and particles. The presence of soot is inherently problematic for the quantification of gaseous precursors, as soot is likely to clog the sampling probe [5,6]. As a result, experiments often involve either gas phase measurements in non-sooting conditions [5–8] or soot measurements in moderate-to-heavy sooting conditions [9-13]. To focus on the inception stage of soot, it is necessary to straddle a middle ground and investigate lightly sooting flames.

A critical variable that contributes to soot formation is pressure. In fact, most practical combustion applications operate at high pressure and soot emissions are exacerbated under these conditions. There has been a rising interest in investigating soot formation in high pressure diffusion flames using the counterflow configuration [9,10,12–14]. This configuration is well-suited because flames are a) resilient to buoyant instabilities [15] and b) onedimensional along the burner axis, which is advantageous from a modeling standpoint and for the identification of the streamline to follow the sequence of the soot formation process. Most of literature on nitrogen-diluted counterflow flames is limited to moderately high pressures (≤ 10 atm) [9,13,14]. Higher pressure flames have been stabilized up to 30 atm by switching to helium dilution [12,15], which, however, can cause secondary effects on soot formation due to preferential diffusion [11] that may complicate the isolation of the effect of pressure.

This work focuses on characterizing incipiently sooting nitrogen-diluted counterflow diffusion flames up to 32atm, including the measurements of 31 gaseous species up to three-ring aromatic and soot volume fraction in the same flame environment. Measurements are performed at 8 atm, 16 atm, and 32 atm by keeping constant stoichiometric mixture fraction and global strain rate to preserve a self-similar flame structure [14] and isolate the effect of pressure on soot formation. Stabilizing a nitrogen-diluted counterflow flame at 32 atm exceeds the highest pressure achieved in past work [5] [6] without the need to resorting to low viscosity diluents (helium) and ensuing complications [12,15,16]. Furthermore, comprehensive measurements encompassing both gas phase and soot in high pressure environments are reported, in contrast to the more limited scope of previous studies. As a result, we anticipate considerable interest in the present database by modelers.

2. Experimental methods

The experimental setup includes a counterflow burner, a chemical analytical system and a digital camera that have all been exhaustively detailed in past work [5,6,17,18]. Only key aspects are briefly summarized here. The burner consists of two converging nozzles with an exit internal diameter of 6.35 mm, surrounded by a nitrogen shroud to shield the flame from external disturbances. Nitrogen diluted ethylene is flowed through the bottom nozzle and nitrogen diluted oxygen from the top nozzle; the two nozzles are separated by a distance $L=8 \,\mathrm{mm}$. A fused silica capillary is inserted radially into the flame and kept under vacuum to extract gaseous samples. The probe tip is positioned near the flame axis and its distance from the blue chemiluminescence is determined by the digital camera, which we use to track and correct any flame dragging because of the probe intrusiveness [6]. To achieve the necessary spatial resolution and resolve the flame structure at high pressures, the probe size is roughly scaled with the diffusive layer thickness [6]. Inner/outer diameter is: $40 \mu m/100 \mu m$ at 8atm, $30 \mu m/130 \mu m$ at 16atm, and $15 \,\mu\text{m}/70 \,\mu\text{m}$ at 32atm. The uncertainty in the position of the probe relative to the blue chemiluminescence of the flame is ± 0.05 mm. The sampling line is coupled to an injection system of a gas chromatograph-mass spectrometer (Agilent 6890A) that is capable of quantifying H₂, O_2 , N_2 , CO, CO_2 and hydrocarbons up to threering aromatics (phenanthrene). Calibrations for all species are done by either bottles (Scotty), mass flow controllers, or electrosprayed liquid solutions in a heated nitrogen flow. We estimate the error of species up to C2 to be $\pm 5\%$ and heavier species to be $\pm 15\%$.

Soot measurements are performed using multicolor pyrometry with a Nikon D70 camera. This technique is well-suited for high pressure environments because, in addition to being non-intrusive, is minimally affected by temperature/density gradients and ensuing beam steering, unlike laser-based alternatives. In addition to soot volume fraction, it provides information on either temperature or optical properties of soot [18]. Pyrometry measurements are performed on the average of 20 images, overlapping the blue chemiluminescence of each image to maintain a spatial resolution of $\pm 16 \,\mu m$. Images are split into the red, green, and blue color channels and deconvolved into a two-dimensional field using an Abel transform. According to Plank's law, the ratio of any two deconvolved color channels, S, can be expressed as

$$\frac{S_i}{S_j} = \frac{\int \eta_i(\lambda) \,\lambda^{-(\alpha+5)} \left[\exp\left(\frac{hc}{\lambda k_B T}\right) - 1 \right]^{-1} d\lambda}{\int \eta_j(\lambda) \,\lambda^{-(\alpha+5)} \left[\exp\left(\frac{hc}{\lambda k_B T}\right) - 1 \right]^{-1} d\lambda}, \quad (1)$$

where λ , h, c, k_B , and α are the wavelength, Plank constant, speed of light, Boltzmann constant and dispersion exponent, respectively. The subscripts i and j represent any one of the three color channels. The CCD sensor spectral response and transmission losses through both the camera lens and pressure-chamber window are accounted for in $\eta(\lambda)$; the spectral response of the sensor is approximately between 375 nm and 700 nm [19]. The dispersion exponent, α , is related to the soot carbonto-hydrogen (C/H) ratio [20,21], and arises from the power-law dependence of the extinction coefficient. Assuming that scattering is negligible compared to absorption and that soot absorptivity is equal to emissivity through Kirchhoff's law ultimately leads to the soot emissivity $\in \propto K_{ext} \propto \lambda^{-\alpha}$ [18,20]. Soot particles are assumed to be in thermal equilibrium with the gas phase and the temperature of the gas phase is based on one-dimensional modeling that has been validated by gaseous species measurements. Consequently, the measured ratio of any two color channels is used to evaluate the dispersion exponent in Eq. (1). Soot volume fraction is evaluated through

$$f_{v} = -\frac{\lambda_{e}}{\tilde{K}_{ext}L_{p}} \ln \left\{ 1 - \epsilon_{c}(\lambda_{e}) \frac{\tau_{e}S_{s}}{\tau_{s}S_{c}} \exp \left[-\frac{hc}{k_{B}\lambda_{e}} \left(\frac{1}{T_{c}} - \frac{1}{T_{s}} \right) \right] \right\},$$
(2)

where λ_e , \tilde{K}_{ext} , L_P , and τ are the effective wavelength of the color channel, dimensionless extinction coefficient, pixel length, and exposure time, respectively. We assume a constant $\tilde{K}_{ext} = 5.34 \pm 2.68$ [18]. The subscripts c and s refer to the calibration and measurements on soot particles, respectively. A S-type thermocouple is used as a light calibration source [22].

One-dimensional modeling is performed using the OPPDIF code [23] and a chemistry model by the CRECK modeling group in Milan (version 2015) [24]). Radiative heat losses by CH₄, H₂O, CO, and CO₂ are included in the energy equation, but soot radiation is neglected. The boundary conditions are summarized in Table 1, including: the molar composition of both fuel and oxidizer streams, mass averaged velocity by assuming plug flow, and computed maximum flame temperature. The momentum flux in the two streams is balanced

Table 1
Boundary conditions for all investigated flames and computed maximum flame temperature.

Pressure	8 atm	16 atm	32 atm
Computed T_{max}	1881 K	1786 K	1697 K
Fuel stream: $V_{\text{avg}} = 7.41 \text{ cm/s}$ at 298 K			
C_2H_4	0.1140	0.1080	0.1000
N_2	0.8860	0.8920	0.9000
Oxidizer stream: $V_{\text{avg}} = 7.30 \text{ cm/s}$ at 298 K			
O_2	0.2438	0.2306	0.2130
N_2	0.7562	0.7694	0.7870

 $(\rho_{fuel}V_{fuel}^2 = \rho_{ox}V_{ox}^2)$. Incipiently sooting flames are meticulously selected for the soot load to satisfy two conflicting requirements: to be compatible with the microprobe sampling technique and be measurable by pyrometry. Additionally, we maintain constant global strain rate (based on the mass average velocity of each stream $a = (V_{fuel} + V_{ox})/L =$ 18.4s⁻¹) and stoichiometric mixture fraction $Z_{st} = (1 + sY_{FF}/Y_{OO})^{-1} = 0.408$. Y_{FF} is the mass fraction of ethylene in the fuel stream and Y_{OO} is the mass fraction of oxygen in the oxidizer stream and s is the mass-based stoichiometric coefficient. Despite the change in inert dilution as pressure is varied, the constancy of a and Z_{st} preserves normalized temperature and gaseous species self-similarity, as reported in [14], shown in the Supplemental Materials (SM) and further discussed below.

3. Results and discussion

We begin the discussion with the spatial profiles of reactants (C₂H₄ and O₂) and major combustion intermediates/products (H2, CH4, CO, CO2, and C_2H_2) in Fig. 1, with symbols representing the experimental measurements and lines the model results. The abscissa is the axial position along the centerline with the origin selected at the position of the gas stagnation plane (GSP). Reactants are depleted at the flame front which is located slightly on the oxidizer side of the GSP. The computed temperature profiles are superimposed in the same figure, reaching a maximum value as tabulated in Table 1 at the flame front and showing a progressively thinning of the flames, as pressure is raised. As already explained, in order to keep the flame soot load at a level compatible with the microprobe sampling technique, the increase in pressure is accompanied by an increase in dilution to lower the peak flame temperature, while keeping constant strain rate and Z_{st}.

The experimental data and computed profiles in Fig. 1 are in good agreement, attesting to the capabilities of the microprobe sampling technique to achieve the necessary spatial resolution to resolve the flame structure even in the flame at the highest pressure. There is a notable, systematic decrease in peak mole fraction of H₂, CO, and C₂H₂ as pressure increases. However, the observed decrease in mole fraction is primarily a consequence of the lower flame temperature, as further discussed in the SM. In the fuel breakdown, hydrogen is stripped from the fuel either by OH or H, OH being the leading contributor at higher pressure [5]. Specifically, C₂H₄+OH accounts for 46% and 59% of vinyl radical (C₂H₃) formation at 8atm and 32atm, respectively, compared to C₂H₄+H that accounts for 49% and 36%, respectively. Despite the dominance of OH attack of the parent fuel, further py-

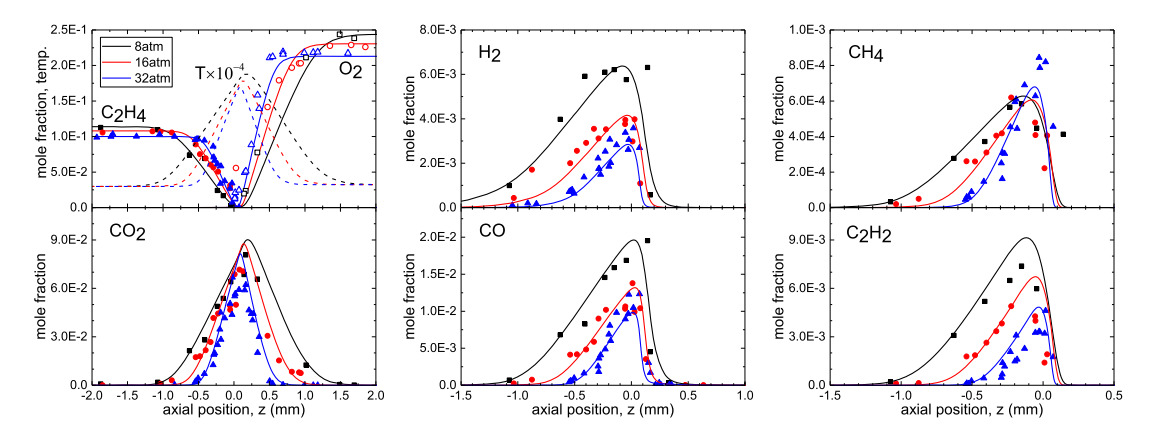


Fig. 1. Spatial profiles of temperature, f mole fractions of reactants and of major intermediates/products.

rolysis of C_2H_3 to form C_2H_2 is overwhelmingly by H-abstraction via H radical (accounting for 93% and 96% of the formation of C_2H_2 at 8atm and 32atm, respectively). While the measured mole fraction of C_2H_4 , C_2H_2 , and H_2 are all well captured by the model, our current GC/MS configuration is unable to quantify H_2O which would help to assess the relative importance of OH and H in the initial fuel breakdown.

To compare directly the flame structure at different pressures and adjust for changes in flame thickness that are a direct consequence of changes in the characteristic diffusive length of the flame, it is instructive to rescale the abscissa. For diffusion flames, the diffusive length is the thickness of the diffusive layer which scales as $\delta \approx \sqrt{D/a}$, where D is the diffusivity, which, in turn, varies with the inverse of pressure, and a is the strain rate [5]. By rescaling the axial coordinate with respect to the diffusive layer thickness ratio, $z \cdot \delta_0/\delta$, the temperature and species profiles become selfsimilar [14]. δ_0 is the reference flame diffusive length at 8atm. Using this scaling stretches spatially the 16atm and 32atm profiles by the square root of the pressure ratio, that is, $\sqrt{16/8}$ and $\sqrt{32/8}$, respectively, and circumvents the need to evaluate the absolute value of the diffusivity for any flame. In addition to the diffusional self-similarity, the temperature-convective time history is the same as pressure is varied (see SM), once the temperature is normalized by the peak temperature. The region where the interesting chemistry takes place to the left of the flame front is characterized by a monotonically decreasing temperature field that is hottest in the 8atm flame, approximately 100 K cooler at 16atm and another 100 K cooler at 32atm. As a result, the flame temperature becomes another controlling variable to be considered in the investigation of the effect of pressure on soot inception. The overall change in fuel and oxidizer stream dilution is 1.4% and 3.1%, respectively. So, the effect of dilution on the concentration of critical species in the soot formation process is inconsequential by comparison with the factor of 4 increase in pressure and $\sim 200 \text{ K}$ change in maximum flame temperature [25].

Following the formation of C_2H_2 , there are two major pathways to yield the first aromatic ring: a C_3H_3 route and a C4/C2 route [1,2]. Intermediates in these pathways are plotted in Fig. 2, the abscissa is the diffusion scaled axial coordinate. As expected in the diffusion scaled coordinate, profiles collapse spatially and only the peak mole fraction is affected by the change in pressure. One exception are the profiles of C₃H₄, with allene and propyne lumped together, which collapse into a single profile well captured by the model at all pressures. While it is known that the resonance-stabilized propargyl radical C₃H₃ is important in aromatic formation, the microprobe sampling technique is limited to quantifying stable species. Nevertheless, quantifying the stable counterpart, C₃H₄, is a reasonable alternative to track the resonance stabilized intermediate radical to aromatic formation. The model qualitatively captures the profile of C₃H₆ at 8 atm but does not predict the six-fold increase in mole fraction as pressure is raised to 32atm. The second major pathway to forming the first aromatic species involves C4 species. The mole fractions of C₄H₄ and C₄H₆ (lumped butadiene and dimethylacetylene) decrease with increasing pressure, a trend that is not captured by the model, even though its predictions are relatively accurate in quantitative terms. C₄H₄ is predominantly formed via $C_2H_2+C_2H_3$, the alternative pathway being a twostep H-abstraction from C₄H₆. Fig. 2 also includes profiles of cyclopentadiene and methylcyclopentadiene which are intermediates of larger aromatics (e.g., naphthalene [1,2]). Methylcyclopentadiene increases with increasing pressure and is well captured by the model; cyclopentadiene, on the other hand, is measured to be independent of pressure and is qualitatively not captured by the model. Nevertheless, on the whole, the model performs reason-

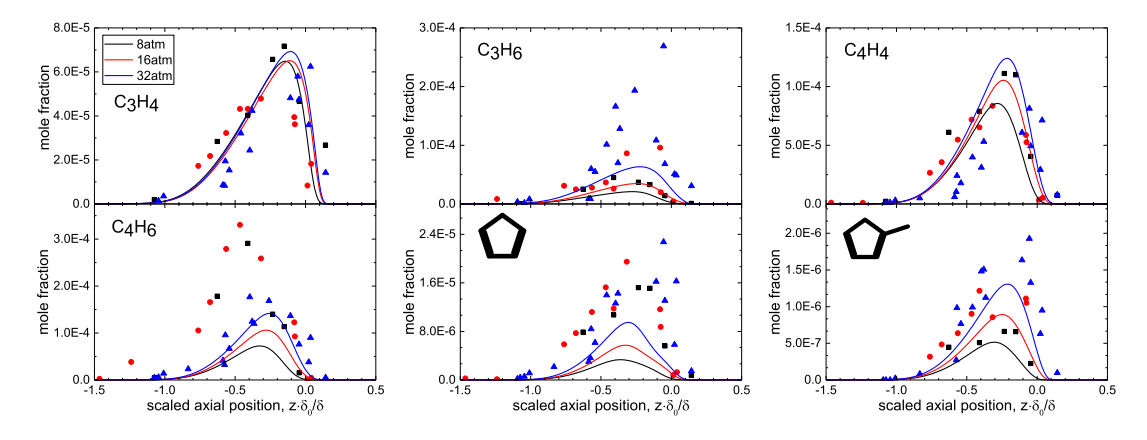


Fig. 2. Spatial profiles of intermediates leading to the formation of benzene. The abscissa is the rescaled axial position.

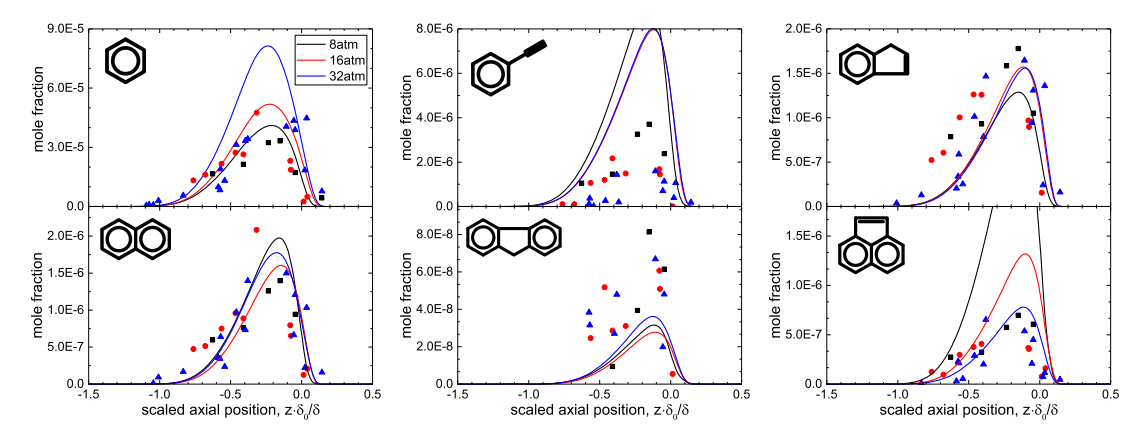


Fig. 3. Spatial profiles of aromatic species. The abscissa is the diffusion-length scaled axial position.

ably well in capturing the critical intermediates in the path to form aromatic species.

We conclude the discussion on the chemical flame structure with the aromatics shown in Fig. 3. The mole fraction of benzene (top left) is measured to be independent of pressure and is overpredicted by approximately a factor of two by the model at 32atm. A reaction path analysis of benzene reveals that the production of benzene is dominated by the C₃H₃ route, but this route becomes less significant at increasing pressures (accounting for 30% of benzene formation at 8atm and 20% at 32atm). The shift at high pressure is due to the more active C4/C2 pathway, accounting for 9% of the formation of benzene at 8atm, increasing to 35% at 32atm. This pressure-dependent shift from C₃H₃ to C4/C2 is consistent with the trends reported in flames up to 8atm [26] and suggests that pressure dependent kinetic pathways, at least up to the formation of benzene, follow a predictable trend in the entire 1–32atm pressure range. The model predictions of C_3H_3 are supported by the experimental data because C₃H₄ is well predicted in all flames. On the other hand, revisiting Fig. 2 we observe that the model does not capture quantitatively C_4H_4 , which may affect the assessment of the significance of the C4/C2 pathway and may explain why the prediction of benzene is less satisfactory at the highest pressure.

Benzene is not the only species that is measured to be independent of pressure. In fact, many species shown in Fig. 3, as well as other aromatics plotted in the SM, exhibit a similar behavior. The collapse of the experimental profiles onto a single one within experimental uncertainty demonstrates the self-similarity of these flames and the level of control that we can achieve. Quantitatively, naphthalene (bottom left) and indene (top right) are well captured and there is reasonable agreement for fluorene (bottom center) which is experimentally more scattered. There are larger discrepancies between experiments and model predictions in many alkylated aromatic species: phenylacetylene (Fig. 3, top center), toluene, xylene, and ethylbenzene (see SM). Acenaphthylene is over predicted by a factor of 5 at 8atm and the agreement at 32atm is likely fortuitous, since trends with pressure qualitatively disagree. From the trends in Fig. 3, one infers that

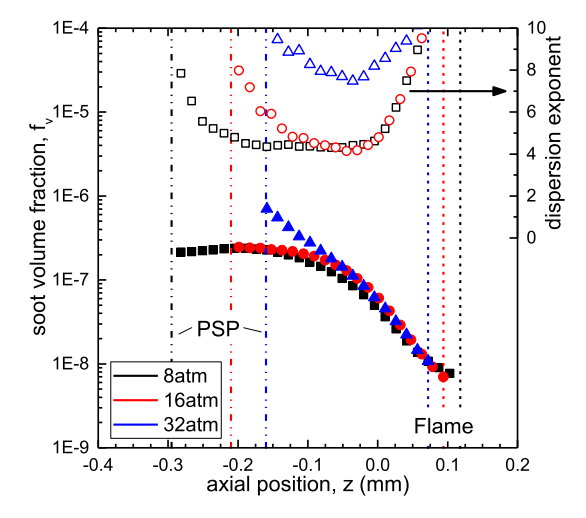


Fig. 4. Soot volume fraction (left ordinate) and dispersion exponent (right ordinate) versus axial position, color coded (online version) on the basis of flame pressure. Vertical lines mark the position of the flame front and particle stagnation plane.

a factor of two increase in pressure equates kinetically a $\sim \! 100\,\mathrm{K}$ decrease in temperature. A total of 31 species have been quantified following the pyrolysis of fuel to 3-ring PAHs: the remaining species profiles are shown in the SM.

The measured soot volume fraction and soot dispersion exponent are shown in Fig. 4. Coupled with the species profile they provide a comprehensive database to examine the effect of pressure on soot formation and its precursors. Vertical lines mark the position of the flame front and particle stagnation plane. Soot nucleates near the flame front and experience subsequent growth as particles are convected toward the particle stagnation plane (PSP) with essentially no opportunity to be oxidized. The flame front coincides with the locations of maximum flame temperature, so particle formation and growth occurs in a monotonically decreasing temperature field. This temperature gradient induces a thermophoretic force that shifts the PSP into the fuel side of the GSP. Despite the difference in flame temperature of the three investigated flames, the measured soot volume fraction profiles collapse in the 0.15mm-thick high-temperature nucleation zone immediately to the left of the flame. These results suggest that in this region the increase in pressure that would cause ordinarily an increase in soot formation is compensated by the decrease of the prevailing temperature, which leaves the measured volume fraction essentially unchanged.

As the flame products are convected from the flame front toward the particle stagnation plane, the volume fraction of the 8atm flame and of the 16atm one remain coincident, whereas the 32atm flame exhibit a comparatively larger growth that will be further discussed below. Furthermore, the results suggest a strong correlation between the

mole fraction of aromatic species (Fig. 3) and soot inception (Fig. 4), both following the same kinetic trends with pressure and temperature.

To discuss further aspects of the soot profiles, we introduce the measured dispersion exponent (α) in the top of Fig. 4 (right ordinate). Soot nucleates with large α values involving highly hydrogenated species. Soot growth is characterized by dehydrogenation [3], causing a decrease in α until plateauing at $\alpha \approx 4$ at 8atm and 16atm, and a minimum of 7 at 32atm. Premixed [20] and diffusion flames in both coflow [27] and counterflow [14] configurations are observed to exhibit a similar plateau in α but the absolute value depends on the flame environment – notably higher at higher pressures. The dispersion exponent increases near the PSP, consistently with measurements in diffusion flames in the 1-8atm pressure range, which was attributed to a low temperature soot nucleation mechanism [14,18]. In particular, this mechanism is likely to be responsible for the already discussed divergence in the soot volume fraction trend at 32atm in correspondence with the rise in α in the region closer to the PSP.

Similarly to our previous work on flames in a lower pressure range [14], the soot production rate, $\dot{\omega}_{soot}$, is calculated using the governing equation for an axisymmetric flow

$$\dot{\omega}_{soot} = \frac{d}{dz} (\rho Y_s (V_{ax} + V_{th} + V_P)) + \rho Y_s \frac{dV_r}{dr}, \quad (3)$$

where ρ and dV_r/dr are the computed local gas density and radial gradient of the radial velocity, respectively. The mass fraction of soot $Y_s = \rho_s f_v/\rho$, is calculated from the *measured* volume fraction from Eq. (2). The density of soot is assumed $\rho_s = 1.5 \text{ g/cm}^3$. Eq. (3) accounts for convec-

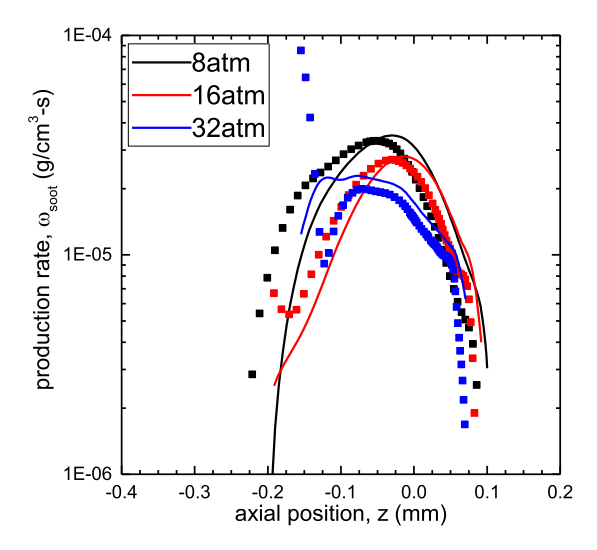


Fig. 5. Soot production rate based on experimentally measured volume fraction. Symbols assume 4 nm particles to estimate Brownian diffusion effects, lines correspond to the limiting case of negligible diffusion.

tive, thermophoretic, and Brownian components $(V_{ax}, V_{th}, \text{ and } V_P, \text{ respectively})$. The effect of Brownian diffusion is assessed by considering monodispersed particles of 4 nm and comparing this case to that in which Brownian diffusion is negligible. The selection of the 4 nm diameter is based on preliminary measurements by light scattering. Further details regarding Brownian diffusion and the effect of particle size are provided in the SM.

As one would expect from the soot volume fraction profiles in Fig. 4, the soot production rate at inception (i.e., near the flame front) is nearly identical in all flames as shown in Fig. 5. The soot production at 8atm is unimodal, initially increasing as one moves from the flame front to the PSP (right to left) with the increase in concentration of PAHs and other soot precursors, then decreasing in vicinity of the PSP as the local flame temperature decreases and Arrhenius based kinetics are suppressed. Brownian diffusion allows back diffusion of particles, resulting in a mere translation of the production curve closer to the PSP and does not have an influence on the peak value if diffusion is neglected. As pressure is raised, there is an inversion of trend near the PSP with the production rate increasing after reaching a local minimum. A similar behavior was reported in counterflow diffusion flames in the 1–8atm at lower Z_{st} [14].

This increase in soot production rate is attributed to a low-temperature soot production mechanism, whereas the first mode is due to the classical high-temperature one. Soot formation in these low temperature and high pressure environments is hypothesized to be dominated by PAH condensation [28]. The low temperature nucleation mechanism seems to be more distinct at atmospheric pressure, activating at temperatures as high

as \sim 1600 K [18], and the activation temperature was observed to decrease with increasing pressure, down to \sim 1400 K at 8atm [14]. We find this transition temperature to be \sim 1285 K and \sim 1200 K at 16atm and 32atm, respectively. The temperature at the PSP of the present 8atm flame is \sim 1375 K, which is too high for this low-temperature mechanism to boost substantially the soot volume fraction, but the contributions of PAHs to soot production/growth are still present, influencing the dispersion exponent and H/C ratio (Fig. 4). As shown in the SM, the transition temperature does not depend on the assumed particle size but diminishes in magnitude as particle size increases.

4. Conclusions

Measurements of gaseous species, including soot precursors, and soot are performed in high-pressure counterflow diffusion flames of ethylene at pressures of 8atm, 16atm, and 32atm, resulting in a comprehensive experimental database that will provide a benchmark for computational models of soot inception at high pressures. To ensure compatibility with diagnostics entailing microprobe sampling and multicolor pyrometry, conditions of comparably light soot loading are chosen carefully as the pressure is raised in twofold increments by offsetting the ensuing pressure-induced increase in soot formation with a $\sim 100 \, \text{K}$ decrease in temperature in the soot forming zone. Under these conditions:

 The profiles of soot volume fraction and of the mole fraction of key aromatic are virtually invariant with pressure in the hightemperature inception zone close to the

- flame. In this region, soot forms with the classic high-temperature mechanism with progressive dehydrogenation, as particles move away from the flame.
- II. As pressure increases (and temperature decreases) the peak production rate of the high-temperature mechanism decreases and, further downstream, a low-temperature mechanism sets in yielding an increase in H/C content, as observed in the 16atm flame and, especially, in the 32atm flame because such a low temperature mechanims becomes progressively more relevant at increasing pressures.
- III. Comparison with the chemistry model showed that, as pressure is raised, the pathway to the formation of the first aromatic ring progressively shifts from the C₃H₃ route to the C4/C2 alternative. This trend that had been observed in the 1–8atm pressure range in a previous study, is now confirmed in the much broader 1–32atm range.

Declaration of Competing Interest

None.

Acknowledgments

The authors acknowledge the support of Yale University and of the National Science Foundation (Grant # 1853150, Dr. Harsha Chelliah, Program Manager).

Supplementary materials

Supplementary material associated with this article can be found, in the online version, at doi:10. 1016/j.proci.2020.06.284.

References

- [1] Y. Wang, S.H. Chung, *Prog. Energy Combust. Sci.* 74 (2019) 152–238.
- [2] H. Richter, J.B. Howard, Prog. Energy Combust. Sci. 26 (4–6) (2000) 565–608.
- [3] B.S. Haynes, H.G. Wagner, *Prog. Energy Combust. Sci.* 7 (4) (1981) 229–273.

- [4] A.E. Karatas, O.L. Gulder, *Prog. Energy Combust. Sci.* 38 (6) (2012) 818–845.
- [5] L. Figura, A. Gomez, *Combust. Flame* 161 (6) (2014) 1587–1603.
- [6] L. Figura, F. Carbone, A. Gomez, Proc. Combust. Inst. 35 (2) (2015) 1871–1878.
- [7] P. Berta, S.K. Aggarwal, I.K. Puri, S. Granata, T. Faravelli, E. Ranzi, J. Propuls. Power 24 (4) (2008) 797–804
- [8] R. Seiser, U. Niemann, K. Seshadri, *Proc. Combust. Inst.* 33 (1) (2011) 1045–1052.
- [9] H.M.F. Amin, A. Bennett, W.L. Roberts, *Proc. Combust. Inst.* 37 (1) (2019) 1161–1168.
- [10] H.M.F. Amin, W.L. Roberts, *Proc. Combust. Inst.* 36 (1) (2017) 861–869.
- [11] R.L. Axelbaum, C.K. Law, W.L. Flower, Proc. Combust. Inst. 22 (1) (1989) 379–386.
- bust. Inst. 22 (1) (1989) 379–386.
 B.G. Sarnacki, H.K. Chelliah, Combust. Flame 195 (2018) 267–281.
- [13] X. Xue, P. Singh, C.J. Sung, *Combust. Flame* 195 (2018) 253–266.
- [14] K. Gleason, F. Carbone, A. Gomez, *Proc. Combust. Inst.* 37 (2) (2019) 2057–2064.
- [15] L. Figura, A. Gomez, *Combust. Flame.* 159 (1) (2012) 142–150.
- [16] U. Niemann, K. Seshadri, F.A. Williams, *Combust. Flame* 162 (4) (2015) 1540–1549.
- [17] F. Carbone, F. Cattaneo, A. Gomez, *Combust. Flame* 162 (11) (2015) 4138–4148.
- [18] K. Gleason, F. Carbone, A. Gomez, *Combust. Flame*. 192 (2018) 283–294.
- [19] P.B. Kuhn, B. Ma, B.C. Connelly, M.D. Smooke, M.B. Long, *Proc. Combust. Inst.* 33 (1) (2011) 743–750.
- [20] S. Torok, V.B. Malmborg, J. Simonsson, A. Eriksson, J. Martinsson, M. Mannazhi, J. Pagels, P.E. Bengtsson, *Aerosol Sci. Technol.* 52 (7) (2018) 757–767.
- [21] R.C. Millikan, J. Opt. Soc. Am. 51 (1961) 698-699.
- [22] B. Ma, M.B. Long, *Proc. Combust. Inst.* 34 (2) (2013) 3531–3539.
- [23] A.E. Lutz, R.J. Kee, J.F. Grcar, F.M. Rupley, OP-PDIF: A Fortran program for computing opposed-flow diffusion flames, Report No. SAND96-8243, Sandia National Laboratories, 1997.
- [24] C. Saggese, S. Ferrario, J. Camacho, A. Cuoci, A. Frassoldati, E. Ranzi, H. Wang, T. Faravelli, *Combust. Flame* 162 (9) (2015) 3356–3369.
- [25] R.L. Axelbaum, W.L. Flower, C.K. Law, Combust. Sci. Technol. 61 (1–3) (1988) 51–73.
- [26] F. Carbone, K. Gleason, A. Gomez, Proc. Combust. Inst. 36 (1) (2017) 1395–1402.
- [27] B. Ma, M.B. Long, Appl. Phys. B Lasers Opt. 117 (1) (2014) 287–303.
- [28] N.A. Eaves, A. Veshkini, C. Riese, Q. Zhang, S.B. Dworkin, M.J. Thomson, *Combust. Flame* 159 (10) (2012) 3179–3190.